2018

Experimental Validation of an Unscented Kalman Filter for Estimating Transient Engine Exhaust Composition with Fourier Transform Infrared Spectroscopy

David Wilson
Marquette University

Casey Allen
Marquette University, casey.allen@marquette.edu

Experimental Validation of an Unscented Kalman Filter for Estimating Transient Engine Exhaust Composition with Fourier Transform Infrared Spectroscopy

David Wilson
Department of Mechanical Engineering, Marquette University, Milwaukee, WI
Casey Allen
Department of Mechanical Engineering, Marquette University, Milwaukee, WI

Abstract

Fourier transform infrared (FTIR) spectroscopy is a prevalent technique for measuring the comprehensive chemical composition of engine emissions. However, its applicability to transient

emissions is limited due to recirculation of exhaust from past engine cycles within a FTIR gas cell and nonstationarity of the infrared beam intensity. An unscented Kalman filter is developed to overcome these limitations and obtain accurate, time-resolved estimations of engine exhaust composition from FTIR measurements. Residence time distribution within the FTIR gas cell is modeled using the well-mixed assumption, while the Fourier transform of an interferogram generated from a linearly evolving, uniformly broadened absorption line is used to deduce transient gas cell composition values from FTIR measurements. The filter utilizes both models, as well as measurement noise statistics, to infer the composition of sample entering the FTIR gas cell during a measurement period. To validate the filter, FTIR measurements of air with transient, trace amounts of acetylene are conducted. A variety of composition profiles are explored with different combinations of composition standard deviation (15 and 45 ppm) and duration between set points (0.4 and 1 s). The results demonstrate that measurement noise becomes less impactful as the magnitudes of composition fluctuations increase, while residence time effects become less significant as the duration of fluctuations increase. Improvements in estimated composition are achieved by the filter in every case, with an average improvement of 32% over unfiltered FTIR measurements. Experiments are conducted using sample flow rates of 12 and 25 standard liters per minute. More accurate measurements and estimations are attained at higher sample flow rates, highlighting the importance of maximizing flow rate to reduce residence time effects for transient measurements.

1. Introduction

Volatile organic compounds (VOCs) significantly impact the overall chemical composition and radiation budget of the atmosphere. An example of a direct impact is the photochemical reaction between VOCs and nitrous oxides (NO_x) to form tropospheric ozone (O_3),[1] a known greenhouse gas. Indirect impacts of VOCs include creating competition for oxidants, thereby increasing the atmospheric lifetime of other greenhouse gases,[2] and by forming secondary aerosols which scatter sunlight and affect cloud droplet formation.[3,4] The extent to which a certain VOC influences the atmosphere depends on its lifetime, reactivity, and reaction mechanisms.[5,6] In addition to atmospheric effects, certain VOCs adversely affect human health,[7] such as benzene which is a known blood carcinogen.[8] According to the National Emissions Inventory, vehicles were responsible for over 23% of anthropogenic VOCs emitted in the United States in 2014.[9]The contribution from vehicles is even larger in urban areas.[10] To improve air quality, future engine control strategies and fuel blends must be optimized to reduce the emissions of targeted VOCs. This task requires the elucidation of the relationships between engine conditions, fuel composition, and the distribution of VOC emissions. Previous research has shown that instantaneous and integrated engine emissions are a function of the speed-load history of an engine for real-world driving conditions,[11,12] which are largely transient.[13] Quasi-steady engine maps, which estimate the emissions of an engine for a given speed/load from steady-state data, neglect these historical effects and provide overly simplified relationships between speed/load and emissions. High-fidelity emissions models must be trained with engine experiments involving real-world speed/load profiles. To properly capture transient and historical effects on VOC distribution from these experiments, a fast measurement technique capable of quantifying many VOCs simultaneously is required. One such technique is Fourier transform infrared (FTIR) spectroscopy.

In FTIR spectroscopy, broadband IR radiation is emitted toward a beam splitter, where half of the beam is reflected/transmitted toward a moving mirror, the other half toward a stationary mirror. The two

beams reflect off their respective mirrors and coalesce at the beam splitter having traveled separate optical path distances. Due to constructive/destructive interference between photons with different wavenumbers, the intensity of the coalesced beam varies as a function of optical path difference. The coalesced beam travels through the sample, contained within the gas cell, where its intensity is reduced due to absorption by the sample. After making multiple passes through the gas cell, the coalesced beam reaches a detector, where its intensity is measured. The measured intensity (interferogram) is then Fourier transformed with respect to optical path difference, yielding a spectrum of intensity vs wavenumber. This spectrum is subtracted from a background spectrum to determine the magnitudes and wavenumbers of absorption by the sample, which are indicative of its chemical composition. A general schematic of a FTIR is shown in Figure 1.

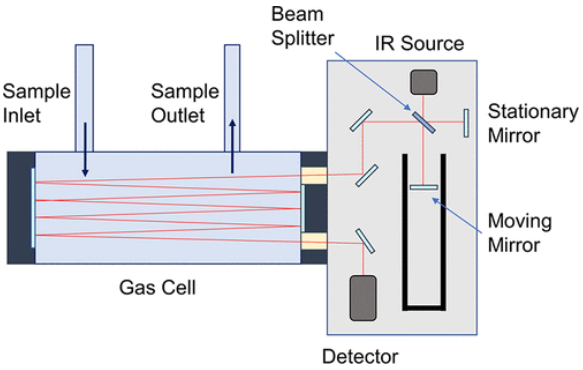

Figure 1. General schematic of a FTIR spectrometer.

FTIR spectroscopy provides many advantages for engine exhaust characterization over other conventional measurement techniques. First, each measurable species has a distinguished spectrum, allowing individual VOCs to be differentiated. On the other hand, individual VOCs can only be measured via flame ionization detection if each VOC is separated using gas chromatography.[14,15] Gas chromatography is a time-consuming process that is typically only performed for batch exhaust samples from entire driving cycles and is therefore unsuitable for time-resolved analysis. Other offline methods such as gas chromatography/mass spectrometry[16] and high performance liquid chromatography[17] also suffer from the similar disadvantages that prevent transient measurements. FTIRs, on the other hand, sample continuously and in real time.

Despite the advantages of FTIR spectroscopy, its suitability for studying engine transients is also somewhat limited. A FTIR gas cell must have sufficient volume to allow multiple passes of the IR beam through the sample. Because of its large volume, residence times within a gas cell can be significantly greater than the measurement period of a FTIR. Consequently, a FTIR gas cell contains exhaust gas from engine cycles extending far into the past, preventing accurate estimations of instantaneous exhaust composition. An illustration of how engine exhaust composition and a FTIR measurement (of total gas cell composition) can differ during a transient is illustrated in Figure 2. Furthermore, there is a limit to which sample flow rate can be increased to reduce residence times before noise addition due to turbulence-induced scintillation becomes an issue.[18] Control of the sample temperature also becomes more challenging as the magnitude of flow rate fluctuations increase. FTIR flow rates for engine exhaust characterization in the literature vary, but are typically between 1 and 12 slpm.[19–27] Another disadvantage of transient analysis with FTIR spectroscopy is that during a transient, the IR intensity at absorbed wavenumbers vary during a measurement period. Fundamentally speaking, Fourier transforms

are only valid for signals that are stationary (statistically independent of time).[28] Spectral calculations from interferograms generated by nonstationary signals are biased, resulting in biased composition estimations, as will be discussed in Section 2.1.2.

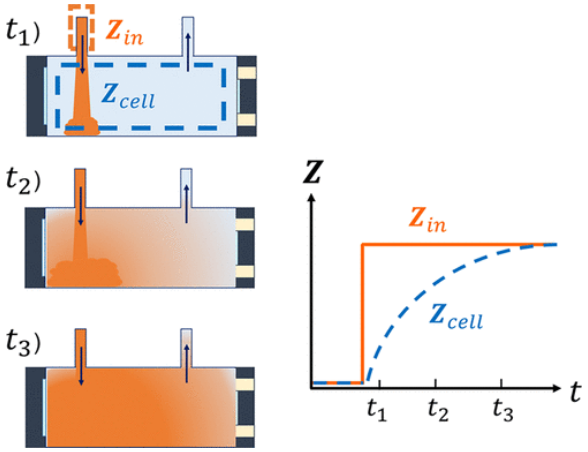

Figure 2. Illustration of how average composition within an FTIR gas cell ($\mathbf{Z}_{\text{cell}}$) evolves due to a step change in sample composition ($\mathbf{Z}_{\text{in}}$). As shown, true sample composition and FTIR measurements can differ substantially.

The residence time issue can be overcome by estimating the composition of sample entering the FTIR gas cell ($\mathbf{Z}_{\text{in}}$ in Figure 2) during a measurement period according to the evolution of the measured total gas cell composition ($\mathbf{Z}_{\text{cell}}$).[23,29] This method requires a residence time distribution model, which provides a relationship between inlet and total gas cell composition. Previous work has shown that the well-mixed model sufficiently represents this relationship for typical flow rates.[30] While this method improves the overall trend in estimated instantaneous engine exhaust compared to raw measurements, noise from the FTIR measurements greatly exacerbates in inlet composition estimations, resulting in considerable errors.[23] However, this issue can be mitigated by filtering FTIR data with a Bayesian estimation model (BEM). BEMs calculate the most statistically probable values for system states (i.e., composition of sample entering a FTIR gas cell) using a system model and known/assumed measurement noise statistics.[31] Since a FTIR gas cell can be modeled as a well-mixed system, the problem of estimating the composition of sample entering a FTIR gas cell is well-suited for Bayesian estimation.

In previous work, an unscented Kalman filter (UKF) for estimating transient composition profiles from FTIR measurements was developed.[30] An UKF is a specific kind of BEM for estimating the states of nonlinear systems, such as an FTIR gas cell represented by a well-mixed model. It is known to be superior to the extended Kalman filter (which performs state estimation by linearizing nonlinear transformations) by at least one order of accuracy[32] and was therefore chosen for this application. The UKF was shown to accurately estimate inlet composition from synthetic FTIR data for a variety of transient profiles. Synthetic FTIR measurements were generated by adding random Gaussian noise to total gas cell composition values calculated from CFD simulations of sample with time-varying composition flowing through a FTIR gas cell. While the results of that work support the use of Bayesian estimation for transient emissions, synthetic FTIR measurements lack the nuance that emerges in true data, such as biasing due to nonstationarity of IR beam intensity at absorbed wavenumbers during a transient. The main priority of this prior work was to demonstrate the biasing effects of sample

recirculation on FTIR measurements and introduce the UKF as a solution to this issue. Biasing due to nonstationarity was not addressed.

Thus, the work presented herein builds on previous work by augmenting the UKF with a modified measurement model which accounts for stationarity effects on FTIR measurements. The modified measurement model is ultimately derived from the Fourier transform of an interferogram generated from a uniformly broadened spectral line with linearly evolving intensity. This derivation demonstrates that the spectrum generated from a transient FTIR measurement, and therefore the corresponding composition, is biased according to the spectral intensity profile with respect to optical path difference during a measurement. In the case of a linear profile, as will be shown, the resulting Fourier transform is more heavily weighted by the intensity at/near small optical path differences. The modified measurement model accounts for this weighting effect to infer the true gas cell composition. Additionally, this work aims to experimentally validate the modified UKF and demonstrate that it improves the estimation of transient sample composition compared the original UKF and unfiltered measurements. These experiments involve introducing mixtures of air/tracer gas with known, transient compositions into a FTIR gas cell and using the UKF to estimate inlet tracer composition from FTIR measurements. The estimated and known tracer composition profiles are compared. Acetylene is used as the tracer gas in this work since it is a VOC that is known to be emitted from engines and is readily available. Experiments are performed for two sample flow rates: 12 and 25 slpm. The first flow rate is typical of the experiments in the literature, while results from the higher flow rate illustrate the benefit of maximizing sample flow rate to reduce residence times within a FTIR gas cell. Tracer composition wave profiles of varying frequencies and amplitudes are presented for both flow rates to simulate transients of varying speeds and magnitudes. Results from spline profiles are also presented, which simulate the irregularities in emissions that occur during real-world driving cycles.

This paper is outlined as follows. First, the key components of the UKF are presented, including the state-space representation of the FTIR gas cell and the measurement model. The issue of biasing due to signal nonstationarity is discussed further, and a modified measurement model for deducing the true gas cell composition from FTIR measurements during transients is proposed. This is followed by a description of the experimental setup for controlling and measuring the flow of tracer gas into the FTIR gas cell. Experimental results are then presented and discussed. FTIR inlet tracer composition profiles estimated from the UKF are compared to the known profiles to evaluate the efficacy of the UKF. The main body of the paper is completed with a set of conclusions and directions for future work. An Appendix is included where the modified FTIR measurement model is thoroughly derived.

2. Methods

2.1. Unscented Kalman Filter Description

In this work, an UKF is implemented to estimate the composition of sample entering a FTIR gas cell to resolve transient composition profiles. The UKF calculates the statistically most probable system states by appropriately weighing model predictions and system measurements according to model uncertainty and measurement error, respectively. Predictions are calculated from the state transition model, which relates current system states to those at the previous measurement time according to the underlying physics of the system. Measurement output is related to the system states by the measurement model. The UKF is chosen over other Bayesian filters since it accurately calculates the statistical distributions of

nonlinear systems.[33] A high-level overview of the UKF is presented, followed by a detailed discussion of the state transition and measurement models for the FTIR gas cell system. Details of the UKF and its fundamental equations are omitted for brevity, but interested readers are referred to the following literature.[30–32]

The UKF was developed based on the idea that approximating a Gaussian distribution is easier than approximating a nonlinear transformation.[33] In this algorithm, the state prediction error and measurement error distributions are represented by a collection of deterministically sampled points, called sigma points, which capture the first and second moments of the distributions. UKFs (and Bayesian filters in general) are comprised of four main steps: state prediction, measurement prediction, gain and update. In the state prediction step, an initial set of sigma points representing the state distribution from the previous measurement time is propagated forward in time according to the state transition model. The new set of transformed sigma points is used to calculate the predicted state values and their error covariances at the current time. An additional term, called the process noise, is added to the calculated error covariance to account for the effects of unmodeled dynamics and model error. Next, the sigma points are transformed again by the measurement model, yielding a prediction of the current measurements and the innovation covariance. Here, innovation is defined as the difference between the actual and predicted measurement values. A term to account for the effects of measurement noise is added to the calculated innovation covariance. In the gain and update steps, the state prediction and innovation, along with their respective distributions, are weighted together to calculate statistically optimized estimations of the current states and their uncertainties. The next two subsections are devoted to the state transition and measurement models, which are essential for generating the prediction and innovation values within the UKF.

2.1.1. State Transition Model

The state transition model provides a physical relationship between the current and previous state values of a system and is a critical element of the UKF. Ultimately, a prediction of sample entering the FTIR gas cell ($\mathbf{Z}_{\mathrm{in}}$) is desired, and the remaining states in the UKF are chosen to assist in its prediction. The three additional states are current and previous total gas cell composition ($\mathbf{Z}_{\mathrm{cell}}$and $\mathbf{Z}_{\mathrm{cell},t-1}$, respectively) and mass flow rate ($\dot{m}$). Total gas cell composition is a strong function of inlet composition. Composition at the previous time step is included in the model because, as will be discussed in the next section, it can influence current FTIR measurements. Mass flow rate is a crucial link in the relationship between inlet and gas cell composition. Equation 1 shown in Chart 1provides the model for each state. Current total gas cell composition is modeled using the well-mixed assumption, which is a function of inlet and total gas cell composition at the previous time. Here, τ represents the effective time constant of the gas cell, defined as the mass within the gas cell divided by mass flow rate. Inlet composition and mass flow are modeled to remain constant throughout a measurement period. These states are modeled this way because the dynamics that influence these states lie outside of the system (are a function of engine operating conditions) and therefore cannot be considered without biasing the predictions. Despite their rudimentary models, accurate final estimations for inlet composition and mass flow rate are obtained during the gain/update steps according to the measurements, total gas cell composition model, and the process noise. The process noise covariance matrix (R_{ww}) approximates the contribution of unmodeled dynamics on the state error distribution and provides additional flexibility for correcting inlet composition and mass flow rate. Variances for inlet composition and mass flow error, denoted Φ_{zin} and $\Phi_{\dot{m}}$ respectively, are estimated/assumed

within R_{ww}. Covariances between Φ_{zin} and $\Phi_{\dot{m}}$ and the error of the other states are approximated using linearization. Values of 100 ppm and 0.25 slpm are used for Φ_{zin} and $\Phi_{\dot{m}}$ in this analysis, as it was determined after trial and error that these values provide adequate estimations for the wide range of profiles explored in this work. The process noise covariance matrix for a single species is given in eq 2 shown in Chart 1. It should be noted that values for $\widehat{\boldsymbol{Z}}_{\text{in}}$, $\widehat{\boldsymbol{Z}}_{\text{cell}}$ and $\hat{\tau}$ in eq 2 are the initial estimations $(t-1|t-1)$. This nomenclature is omitted for brevity. It should also be noted that for the UKF to perform adequately, estimations of the initial states $\hat{x}(0)$ must be reasonably accurate. Thus, the first measurement that the UKF processes should occur during steady-state, when the inlet and gas cell compositions are equal and steady, enabling the compositions to be unequivocally deduced from the FTIR measurement.

Chart 1

$$\hat{x}(t|t-1) = \begin{bmatrix} \widehat{\boldsymbol{Z}}_{in}(t|t-1) \\ \widehat{\boldsymbol{Z}}_{cell}(t|t-1) \\ \widehat{\boldsymbol{Z}}_{cell,t-l}(t|t-1) \\ \hat{\dot{m}}(t|t-1) \end{bmatrix}$$

$$\begin{bmatrix} \widehat{\boldsymbol{Z}}_{in}(t-1|t-1) \\ \widehat{\boldsymbol{Z}}_{in}(t-1|t-1)\left(1-e^{-\frac{\Delta t}{\hat{\tau}(t-1|t-1)}}\right) + \widehat{\boldsymbol{Z}}_{cell}(t-1|t-1)\, e^{-\frac{\Delta t}{\hat{\tau}(t-1|t-1)}} \\ \widehat{\boldsymbol{Z}}_{cell}(t-1|t-1) \\ \hat{\dot{m}}(t-1|t-1) \end{bmatrix}$$

(1)

$$R_{ww}(t-1)$$

$$= \begin{bmatrix} \Phi_{z_{in}} & \Phi_{z_{in}}\left(1-e^{-\frac{\Delta t}{\hat{\tau}}}\right) & 0 & 0 \\ \Phi_{z_{in}}\left(1-e^{-\frac{\Delta t}{\hat{\tau}}}\right) & \Phi_{z_{in}}\left(1-e^{-\frac{\Delta t}{\hat{\tau}}}\right)^2 + \Phi_{\dot{m}}\left[\frac{\Delta t}{m} e^{-\frac{\Delta t}{\hat{\tau}}}\left(\hat{Z}_{in}-\hat{Z}_{cell}\right)\right]^2 & 0 & \Phi_{\dot{m}}\frac{\Delta t}{m} e^{-\frac{\Delta t}{\hat{\tau}}}\left(\hat{Z}_{in}-\hat{Z}_{cell}\right) \\ 0 & 0 & 0 & 0 \\ 0 & \Phi_{\dot{m}}\frac{\Delta t}{m} e^{-\frac{\Delta t}{\hat{\tau}}}\left(\hat{Z}_{in}-\hat{Z}_{cell}\right) & 0 & \Phi_{\dot{m}} \end{bmatrix}$$

(2)

2.1.2. Measurement Model/FTIR Measurement Bias

The measurement model describes the relationship between system states and measurement output and allows the innovation and its statistics to be calculated. Observations of the system are provided by

two measurement devices: a mass flow meter and a FTIR. Mass flow rate is directly measured by the flow meter, yielding a straightforward measurement model. The relationship between FTIR measurements and gas cell composition is more complicated, especially for transients. For steady-state measurements where the composition within the gas cell is unchanging, the measurement model is simply the conversion of gas cell mass fraction to mole fraction, since FTIRs are calibrated at steady state to yield mole fractions from spectral intensity of the IR beam according to the Beer–Lambert law.[34] However, changes in spectral intensity due to evolving composition during a measurement period introduce bias into the calculations of spectral intensity for broadened absorption lines. The spectral intensity of broadened absorption lines calculated by the Fourier transform is NOT the average value of spectral intensity during a moving mirror scan, but rather is biased according to the profile of the spectral intensity with respect to optical path difference of the split beams, which varies with moving mirror position. To further complicate things, the direction of the moving mirror scan alternates each measurement period in many commercial FTIRs. While this doubles the measurement frequency of the instrument (the repositioning of the moving mirror to the initial location is utilized as an additional scan), the profiles of moving mirror position relative to time are reversed for each measurement. This convolutes the task of determining composition profiles with respect to time from FTIR measurements.

To illustrate the complexities of FTIR measurements during transients, consider Figure 3 which shows FTIR measurements during a step change in inlet tracer composition from approximately 70 ppm to 170 ppm at 12 slpm. Overall, the FTIR measurements follow approximately an exponential curve as expected. However, the measurements exhibit period-dependent behavior, where the composition output alternates between significant and gradual rise. These anomalous oscillations in the FTIR measurements cause the estimated inlet composition values from the UKF to oscillate as well, yielding severe errors. The cause of these oscillations is the alternation of the moving mirror direction for each measurement. Mathematical analysis, outlined in detail in the Appendix, reveals that for a broadened spectral line with linearly changing ensemble-averaged intensity, the value calculated by the Fourier transform is heavily weighted by the intensity at/near the centerburst location. Here, the centerburst location is defined as the initial moving mirror position where it is equidistant from the beamsplitter as the stationary mirror, resulting in complete constructive interference between the split beams. The effect of this centerburst weighting is illustrated in Figure 4. For a forward scan (from centerburst to maximum optical path difference), the centerburst occurs at the beginning of the scan. Therefore, the measured composition for a forward scan is heavily weighted by the composition at the beginning of the scan for a transient measurement. Conversely, the centerburst occurs at the end of the scan when the mirror moves in the backward direction, yielding a measured composition that is heavily weighted by the composition at the end of the scan. Periods of gradual rise in the FTIR measurements in Figure 3 occur between successive backward/forward scans, since the centerburst position for these two scans occur closely together in time. Conversely, periods of significant rise occur for successive forward/backward scans, due to the centerburst locations being separated by two full scans.

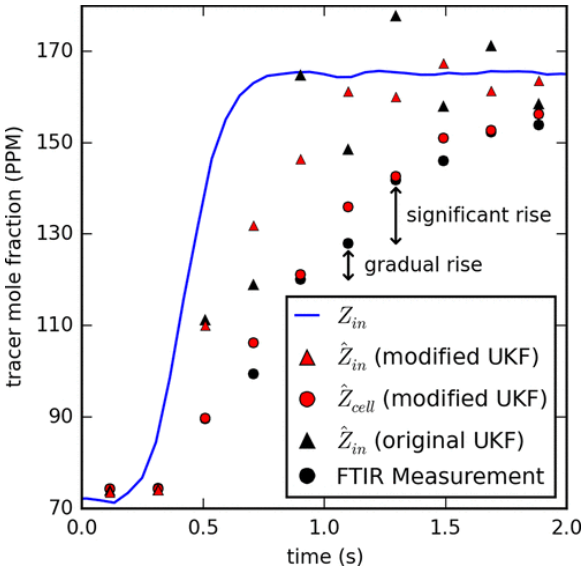

Figure 3. Estimated tracer inlet composition from the modified (red) and original (black) UKF. The modified UKF accounts for period dependent behavior of FTIR measurements.

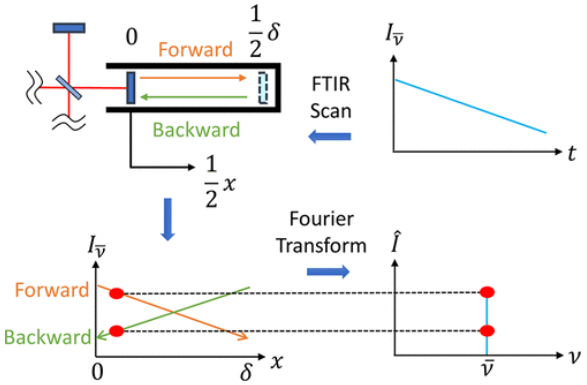

Figure 4. Illustration of how scan direction can affect FTIR output. The upper right figure shows the linearly diminishing intensity (I) of a broadened line with respect to time (t) centered at wavenumber $\bar{\nu}$. Different intensity values are calculated by the Fourier transform depending if the mirror is scanning in the forward or backward direction. The variables x and δ represent optical path difference and maximum optical path difference, respectively.

A modified measurement model for FTIR output is proposed to account for the effects of centerburst weighting during transient FTIR measurements. This model provides an approximate relationship between the composition measurements from the FTIR and the true composition at the beginning/completion of a scan. The measurement model is given in eq 3 shown in Chart 2. Different models are applied to each scan direction, since the FTIR output is heavily weighted by the composition at the centerburst location but is also relatively weakly affected by the composition at the maximum optical path difference location. For a forward scan, the composition at the previous measurement time is used as the centerburst composition, since the centerburst occurs at the beginning of the scan, which is close in time to the completion of the previous backward scan. The current composition is used as the centerburst composition for a backward scan, since the centerburst occurs at the completion of a backward scan. $\mathbf{MW}$ and $\mathrm{MW_{mix}}$ represent the molecular weights of the species of interest the total gas cell sample, respectively. The molecular weight of the mixture in eq 3 can be calculated using the gas

cell composition distribution within the UKF, which should include the major species CO_2 and H_2O in engine applications since these are measured by the FTIR. The composition of N_2, the other major constituent, can be approximated by subtracting the composition of CO_2 and H_2O from 1. VOC composition can be factored into the calculation as well if more accuracy is desired. In this work, gas cell molecular weight is simply approximated with the molecular weight of air. Details of the derivation of the FTIR measurement model are in the Appendix. Measurement noise variance for this work is approximated by filling the gas cell with approximately 100 ppm of acetylene and taking continuous measurements over a 3 min span. The variance of these measurements is approximately 1.5 ppm.

Chart 2

$$\hat{y}(t|t-1) = \begin{bmatrix} \begin{cases} \left[Z_{cell,t-1}(t|t-l) + \dfrac{Zcell(t|t-1) - Z_{cell,t-1}(t|t-1)}{2\pi Si(2\pi)} \right], \dfrac{MW_{mix}}{\boldsymbol{MW}} & \text{forward scan} \\ \left[Z_{cell}(t|t-l) + \dfrac{Zcell(t|t-1) - Z_{cell,t-1}(t|t-1)}{2\pi Si(2\pi)} \right], \dfrac{MW_{mix}}{\boldsymbol{MW}} & \text{forward scan} \end{cases} \\ \dot{m}(t|t-1) \end{bmatrix} \quad (3)$$

2.2. Experimental Setup

Experimental validation of the UKF is performed by flowing known quantities of tracer gas through a FTIR gas cell and comparing the known tracer compositions to those estimated by the UKF. These experiments require an architecture for controlling tracer flow and a FTIR spectrometer for measuring composition. The FTIR utilized for this study is the MKS 2030-HS. The MKS 2030-HS has a gas cell with a volume of approximately 200 mL and measures at a high frequency of 5 Hz, allowing transient composition profiles to be reasonably captured. However, the extent to which transient profiles can be captured is limited by the factors outlined in Section 2.1.2, namely, residence time effects and nonstationarity of the intensity of the IR beam. The MKS 2030-HS has a spectral resolution of 0.5 cm^{-1} and an IR path length of 5.11 m. A low spectral resolution allows absorption lines in close proximity to be resolved, while the long path length permits low-level detectability. The FTIR is equipped with silicon carbide radiation source at 1200 °C, a liquid nitrogen-cooled mercury cadmium telluride detector, and a helium neon laser for generating a reference interferogram. A temperature of 191 °C is maintained within the FTIR gas cell and the upstream sample line with the aid of a controller. Temperature and pressure within the gas cell are measured and reported at a frequency of 5 Hz.

The tracer gas chosen for these experiments is acetylene. Acetylene is introduced into the FTIR using a MKS GM50A mass flow controller (MFC) with a 0–40 sccm flow range. The flow controller is accurate to within 1% from 20% to 100% full scale and has a reported settling time of less than 750 ms. Flow rate commands are received by the MFC from LABVIEW at approximately 50 ms intervals. The MFC is connected to a manifold, which also draws in room air due to suction from a pump downstream of the FTIR. Acetylene/air is drawn into the FTIR, where the acetylene mole fraction within the FTIR gas cell is measured. Downstream of the FTIR is a valve, which is used to set the flow rate, followed by a MKS GM100A mass flow meter (MFM). The MFM is capable of measuring flow rates from 2 slpm to 100 slpm, with 0.2% accuracy from 2 to 20 slpm, and 1% accuracy from 20 to 100 slpm. Acetylene mass fraction of

the sample is calculated by dividing the acetylene flow rate from the MFC by the total sample flow rate measured by the MFM. To directly compare estimated FTIR inlet composition from the UKF with the known composition from the MFC/MFM data, the time-lag between the introduction of tracer from the MFC to the tracer reaching the FTIR must be considered. This time-lag is estimated by dividing total volume of the line between the MFC and FTIR by the volume flow rate, corresponding to time-lags of approximately 0.5 and 0.25 s for flow rates of 12 and 25 SLPM, respectively. A diagram of the setup is shown in Figure 5.

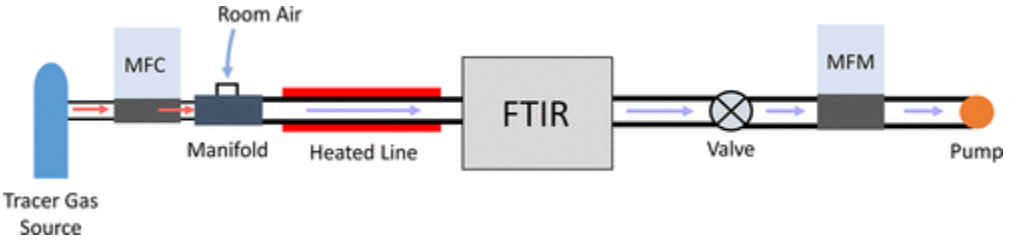

Figure 5. Experimental setup for UKF validation.

3. Results and Discussion

Presented in this section are experimental results for the validation of the modified UKF. The ability of the UKF to estimate transient engine emissions from FTIR measurements is evaluated by flowing samples with known, transient tracer composition through the FTIR gas cell. Estimated tracer composition from the UKF is compared to the known composition profiles. It is shown that the UKF yields significant improvements over unfiltered FTIR measurements, which are susceptible to residence time and stationarity issues. Measurements are presented along with error bars to reflect their uncertainty due to quantification/calibration errors. This uncertainty value is provided by MKS and is estimated to be approximately 2% of the measured composition for 95% confidence. The UKF is validated over a wide range of transient profiles to ensure its robustness. First, results for wave profiles at frequencies ranging from 0.75 to 1.5 Hz are presented. Different frequencies are investigated to explore the relationship between filter performance and transient duration and to determine the duration limit at which a fluctuation in emissions can be adequately captured. The amplitudes of these waves are varied from 10 to 100 ppm to explore the relationship between filter performance and magnitude of emissions fluctuations, and how measurement noise can mask fluctuations of smaller magnitude. To simulate real-world emissions profiles, experiments are conducted for spline tracer profiles, where the tracer set points are randomly selected from a distribution. The results of these experiments demonstrate the ability of the UKF to predict complicated emissions profiles. To explore the effects of duration and magnitude of emission fluctuations on estimates from the UKF, experiments are conducted for spline profiles with varying scales and time between set points, respectively. More detail on the spline profiles is provided in Section 3.2. Experiments are conducted at sample flow rates of 12 and 25 slpm. The former flow rate is typical for FTIR measurements of engine exhaust in the literature. However, residence times within the FTIR gas cell are shorter at higher flow rates, reducing historical effects and resulting in measurements that more accurately reflect true transient emissions profiles. Experiments are conducted at the higher flow rate to demonstrate this benefit.

Although engine emissions profiles in real-world driving scenarios vary considerably according to engine type, fuel, and driving cycle, the magnitudes of emissions fluctuations explored in this work resemble those of some engine studies found in the literature. For example, Gierczak et al. measured VOC

emissions from a flex-fuel vehicle during a FTP cold start, and found that acetaldehyde, ethanol, and formaldehyde emissions varied from 0 to approximately 150, 100, and 10 ppm, respectively.[19] In an investigation of VOC emissions from a gasoline engine operating with different blends of alcohol during the NEDC driving cycle, propylene and ethanol emissions spiked on the order of 100 ppm during the first transient event, while formaldehyde, 1–3 butadiene, benzene, and toluene spikes ranged between 30 and 70 ppm.[35] Acetaldehyde and formaldehyde emissions from a four-stroke gasoline-powered motorcycle regularly fluctuated on the order of 100 ppm during a transient driving cycle in work by Penteado et al.[36] The durations of emission fluctuations also vary substantially in the literature. For example, measurements of total HC emissions from a GDI engine under the NEDC driving cycle using a fast response chemiluminescence detector showed fluctuations on the order of thousands of ppm with durations ranging from milliseconds to several seconds.[37] The experiments in this work cover an intermediate portion of this duration range, as the lowest duration at which a transient event can be measured is limited by the FTIR measurement frequency, which is 5 Hz. Furthermore, previous analysis demonstrated that inlet composition profiles that fluctuate at frequencies greater than 1.25 Hz are inadequately captured at this measurement frequency.[30] This finding guided the selection of transient profiles explored here.

3.1. Tracer Wave Profile Results

Shown in Figure 6 are results for wave profiles with frequencies ranging from 0.75 to 1.5 Hz at a sample flow rate of 12 slpm. Generally, the estimated inlet composition from the UKF follows the true composition more closely than unfiltered FTIR measurements. The unfiltered FTIR measurements fail to capture the extremes and lag the inlet composition profiles due to residence time effects. The UKF, however, leverages measurement changes and state/measurement models to accurately calculate changes in inlet composition. In most cases, better estimations are obtained when the inlet profile has greater amplitudes and lower frequencies. For example, comparing Figure 6a,e,i, which corresponds to amplitudes of 100, 25, and 10 ppm for the lowest frequency, respectively, it is seen that as amplitude decreases more erroneous estimations appear. Although accurate estimations of amplitude are attained in Figure 6e, there are a few artifacts in the estimated profile, such as the sudden increase in composition near 4.5 s when the true composition is at a trough. At about 3.5 s in Figure 6i, there is a sudden decrease in estimated composition when the true composition reaches a peak. These anomalous estimations occur because as amplitude decreases, the magnitude of measurement changes become comparable to that of the measurement noise, masking the true composition profile. Nevertheless, the UKF generally improves the estimations of inlet composition and provides more accurate estimations of the extremes of the profile, even for some of the 10 ppm cases. It should be noted that the true inlet composition for the smaller amplitudes, especially the 10 ppm cases, appear relatively noisy. This is due to resolution and settling time limitations of the mass flow controllers that prevent accurate control for small set points changes and may contribute to some of the measurement/estimation errors seen for these cases.

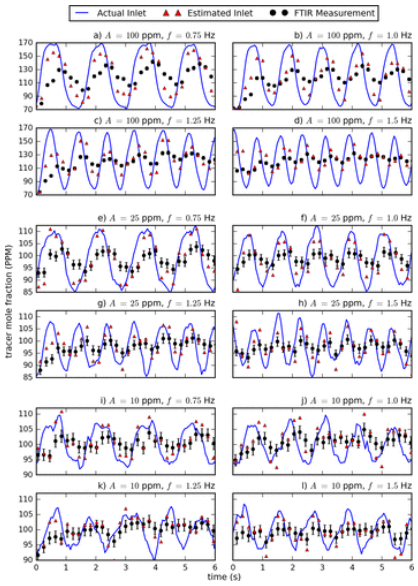

Figure 6. Estimations from the UKF of acetylene inlet composition vs FTIR measurements. The frequencies and amplitudes of the transient composition profiles vary from 0.75 to 1.5 Hz, and 10 to 100 ppm, respectively. The sample flow rate is 12 slpm.

As frequency increases beyond 0.75 Hz, the quality of the estimations from the UKF generally deteriorates, and the peaks of the inlet composition profile are less accurately estimated. This is clearly seen when comparing Figure 6e,f, which correspond to the 0.75 and 1.0 Hz profiles with 25 ppm amplitudes, respectively. The fact that better estimations are obtained for lower frequencies is partly attributed to the relatively large residence times of sample within the gas cell, which causes the total gas cell composition (or FTIR measurements) to lag the inlet composition. This lagging effect becomes more significant as inlet composition frequency increases, since the total gas cell composition profile has less time to catch up with inlet composition profile before it changes trajectory. This is seen in Figure 6d, where the amplitude of the measurement profile is significantly less than that of the inlet composition profile for the 100 ppm, 1.5 Hz case. Furthermore, the ability to estimate high frequency transients is also limited by the measurement frequency. As the ratio between inlet composition and measurement frequency increases, the magnitude of sampling errors becomes greater since inlet composition changes more significantly between measurements. Nevertheless, the UKF generally yields better estimations of the inlet composition profile than the raw measurements, even for the higher frequency cases.

Figure 7 shows data for wave inlet composition profiles for experiments conducted at a sample flow rate of 25 slpm. Many of the trends from the 12 slpm cases are also seen in Figure 7, namely, that lower frequency and higher amplitude result in better estimations. However, more accurate estimations of the amplitudes of the transient inlet composition profiles are generally obtained for the 25 slpm cases when compared with their counterparts in Figure 6. This is due to residence time being reduced at higher flow rates. With a lower residence time, the old sample within the gas cell is displaced more quickly, and the total gas cell composition profiles resemble the inlet composition profiles more closely. This is seen by comparing the measurements in Figures 6d and 7d, which correspond to the 100 ppm, 1.5 Hz cases. For the higher flow rate case, the extremes of the measurement profile are closer to those of the inlet composition profile, which results in the extremes of the inlet composition profile to be more accurately calculated in general. However, even at the higher flow rate, the effects of lagging are still apparent, and

measurement frequency limitations still apply. This is especially true for the high frequency inlet composition cases. The effects of lagging for the higher flow rate cases will be discussed in more detail in Section 3.2.

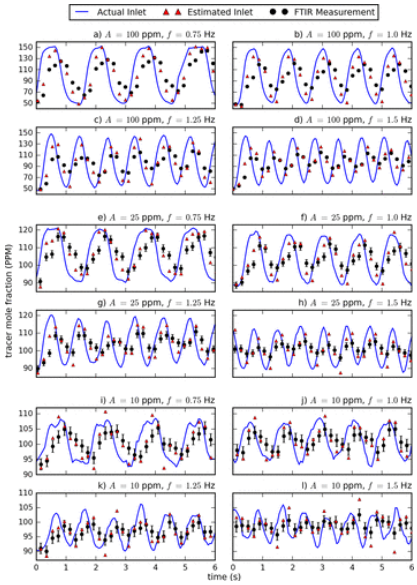

Figure 7. Estimations from the UKF of acetylene inlet composition vs FTIR measurements. The frequencies and amplitudes of the transient composition profiles vary from 0.75 to 1.5 Hz, and 10 to 100 ppm, respectively. The sample flow rate is 25 slpm.

3.2. Spline Profile Results

Emissions profiles from vehicles undergoing real-world driving cycles, which contain irregular periods of acceleration and deceleration, likely do not resemble to the wave profiles from the experiments presented in Figures 6 and 7. To simulate more realistic emissions profiles, experiments are conducted for inlet composition spline profiles generated from randomly selected set points within a distribution. Two sets of five spline profiles are used for these experiments, totaling 10 profiles. In the two sets of profiles, set points are separated by 0.4 and 1 s, respectively. Profiles with distinct set point separations (t_s) are used to investigate how performance of the UKF changes with respect to the duration of composition fluctuations. To ensure that the composition profile is relatively smooth and contains minimal steady-state portions, one interpolation point is used midway between set points. This is especially necessary for the set of profiles where t_s is 1 s, as this is less than the settling time of the mass flow controllers. To avoid having two consecutive set points within the resolution limit of the flow controllers, a set point remains unchanged if its randomly selected value is within 1/3 of a standard deviation of the previous set point. This ensures stability of the flow controller. The spline profiles are presented in Figure 8. Green and gray lines correspond to profiles where t_s is 0.4 and 1 s, respectively. To investigate how the magnitude of emissions variations affects filter performance, two sets of experiments with different scales are conducted for each spline profile. The standard deviations of the set points (σ_{zin}) for both experiments are 15 and 45 ppm, respectively. Thus, inlet composition in the figure is expressed as the difference from the mean inlet composition in terms of standard deviations. As in the wave profile cases, two sets of experiments are conducted for each profile/magnitude combination at sample flow rates of 12 and 25 slpm, respectively. Two trials are conducted for each experiment.

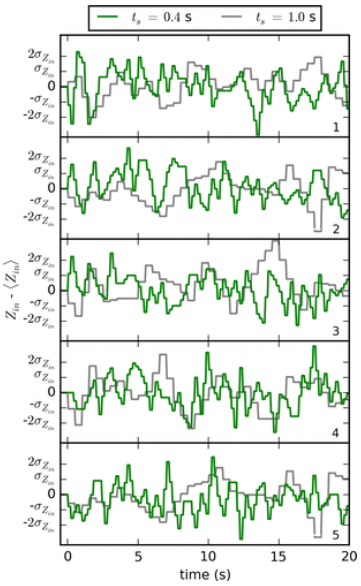

Figure 8. Transient inlet tracer composition spline profile set points expressed in terms of standard deviations from the mean.

Figure 9 shows results for inlet composition profile 1 of the 0.4 s interval cases for both inlet composition standard deviations and flow rates. In general, the estimated inlet composition from the UKF follows the true inlet composition profile more closely than the unfiltered FTIR measurements. Similar trends as those found in wave profiles are also found in the spline profiles. The peaks and troughs of the unfiltered FTIR measurements are more representative of that of the inlet composition profiles for the higher flow rate cases, due to decreased residence time. As a result, the peaks and troughs of the estimated inlet composition profiles for the high flow rate cases are more accurate as well. This is apparent, for example, when comparing estimations of the first peak from Figure 3c,d, which correspond to the 12 slpm and 25 slpm cases where σ_{zin} is 45 ppm. The estimation in the low flow rate case reaches only about 70% of the true apex, while the high flow rate estimation reaches within a few percent. Qualitatively, fewer anomalous oscillations in estimated inlet composition appear for the cases with higher flow rates and magnitudes of inlet composition changes. This is seen when comparing Figure 9a (the 15 ppm, 12 slpm case) with the remaining cases in the figure. While the estimations from the UKF are an overall improvement from the raw FTIR measurements for this case, there are a few instances where the estimated profile increases when the true profile decreases and vice versa. Measurement noise is ultimately responsible for these oscillations. Cases with lower flow rates/composition fluctuations are more susceptible to measurement noise effects since the ratios between measurement changes and noise are lower.

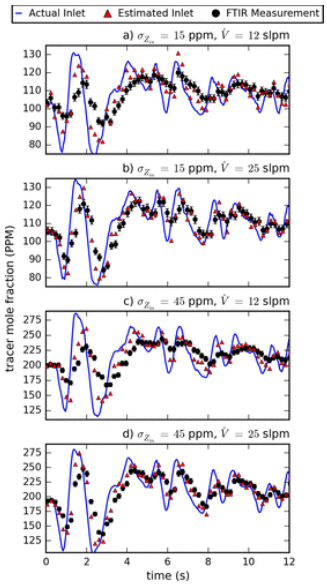

Figure 9. Estimations from the UKF of acetylene inlet composition vs FTIR measurements for the first 12 s of spline profile 1 of the t_s = 0.4 s set. Each window presents results for distinct values of $\dot{V}$ and σ_{zin}.

Shown in Figure 10 are results for inlet composition profile 1 of the cases where σ_{zin} is 1 s. Many of the same observations from the spline cases with lower duration between set points can be discerned from the data in Figure 10. Peaks and troughs are more accurately captured in the high flow rate cases, and the effects of measurement noise are appreciable for the 15 ppm, 12 slpm case. The key difference between the results from the two sets of profiles is that the lag between inlet composition and FTIR measurement profiles is less significant for the 1 s interval cases, resulting in more accurate overall estimations for inlet composition. Since the inlet composition changes trajectory less frequently for these cases, the total gas cell composition/FTIR measurements have more time to respond to inlet composition transients.

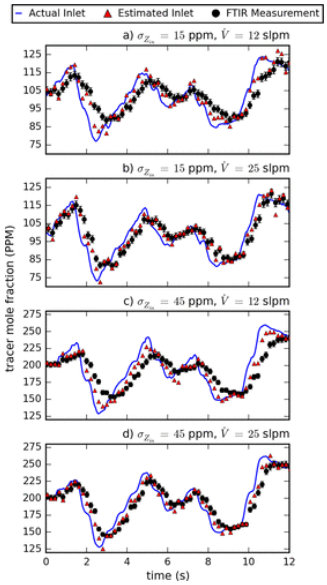

Figure 10. Estimations from the UKF of acetylene inlet composition vs FTIR measurements for the first 12 s of spline profile 1 of the t_s = 1 s set. Each window presents results for distinct values of $\dot{V}$ and σ_{zin}.

To quantify the performance of the UKF for the spline inlet composition profiles and support some of the qualitative observations made in previous paragraphs, data from the spline experiments are consolidated according to flow rate, inlet composition magnitude, and duration between set points. The data are presented in Figure 11, which shows the average absolute error in estimated inlet composition over all experiments for each category. Average absolute difference between FTIR measurements and true inlet composition is also presented, which serves as a benchmark to which inlet composition estimations are compared. The UKF significantly improves the estimation of the transient inlet composition profile compared to the raw FTIR measurements in every case. A maximum improvement of 45% is achieved for the case where $\dot{V}$ = 12 slpm, σ_{zin} = 45 ppm, and t_s= 1 s, while the case with a minimum improvement is the $\dot{V}$ = 25 slpm, σ_{zin} = 15 ppm and t_s = 0.4 s case at 26%.

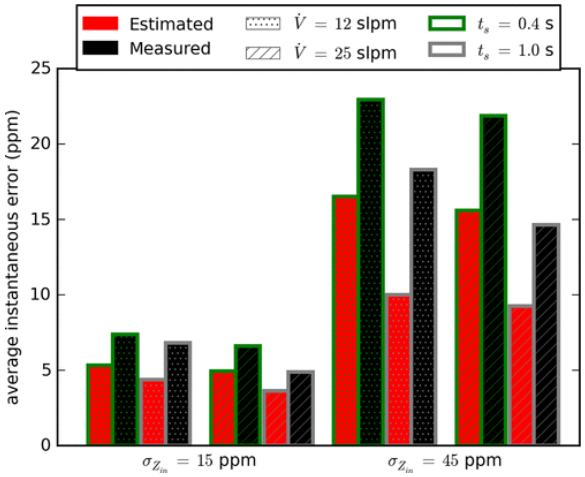

Figure 11. Average error in instantaneous acetylene inlet composition calculated from the UKF (red) and unfiltered FTIR measurements (black) for distinct values of t_s, $\dot{V}$, and σ_{zin}.

Figure 11 also illustrates some interesting trends for filter performance with respect to the various categories. Lower measurement and estimation errors are achieved for the transient profiles with a t_s value of 1 s compared to that of 0.4 s. The average deviation between FTIR measurements and true inlet composition values is 11.15 and 14.7 ppm for t_s values of 1 and 0.4 s, respectively. For transient profiles with fluctuations of shorter duration, FTIR measurements have insufficient time to respond to these fluctuations, which leads to estimations with greater error. The UKF is also more effective for cases where inlet composition fluctuations are of greater magnitude. On average, the UKF improves the estimated composition profile by 29% and 35% for the cases where σ_{zin} is 15 and 45 ppm, respectively. This is expected, since measurement noise is more comparable to the magnitude of FTIR measurement fluctuations for the 15 ppm cases. Figuratively speaking, the UKF is hesitant to update the inlet composition estimation based on measurement changes of small magnitude, since noise could be a primary contributor to the measurement change. This contributes to the lagging effect and results in estimation errors. Lastly, increasing flow rate from 12 to 25 slpm decreases measurement and estimation error by 10% and 8% on average, respectively. At higher flow rates, residence times within the gas cell are reduced, leading to measurements and estimations that more accurately reflect the true inlet composition.

The improvement in estimated composition from the UKF compared to unfiltered measurements exceeds the uncertainty due to quantification error (~4 ppm) in each of the σ_{zin} = 45 ppm cases.

However, for the lower fluctuation cases, the improvement is comparable to the uncertainty due to quantification error (∼2 ppm). Out of all the low fluctuation cases, the best improvement of 2.4 ppm is achieved for the t_s = 1 s, $\dot{V}$ = 10 slpm case, while the lowest improvement of 1.2 ppm is attained when t_s = 1 s and $\dot{V}$ = 25 slpm. While the average estimation improvements for the low fluctuation cases are near/within the quantification uncertainty, it is important to note that the estimation of relative composition trends are nevertheless substantially enhanced by the UKF. The magnitudes of the composition fluctuations are accurately captured by the UKF estimations, as demonstrated in Figures 6, 7, 9, and 10. Estimations of fluctuation magnitudes are essentially unaffected by systematic errors in the quantification, which simply offset the FTIR measurements by a fixed amount. Thus, the UKF is nevertheless valuable for inferring transient emission trends.

4. Conclusion

A UKF for obtaining time-resolved estimations of the composition of engine emissions from FTIR measurements is formulated. This filter overcomes the issues of residence time distribution within a FTIR gas cell and nonstationarity of the IR intensity which typically limits the ability of FTIRs to accurately measure transients. The UKF utilizes a well-mixed model of the FTIR gas cell to infer the inlet composition based on evolution of the measurements. A measurement model accounts for the effects of nonstationarity on the FTIR measurements by utilizing the Fourier transform of an interferogram generated from a uniformly broadened absorption line with linearly evolving intensity. The UKF is experimentally validated by flowing sample with transient acetylene composition through a FTIR. It is demonstrated that the UKF accurately estimates the composition of sample entering the FTIR gas cell during a measurement period and therefore can be extended to resolve FTIR measurements of transient engine emissions. The following is a list of conclusions from this study.

- The UKF is shown to reproduce wave composition profiles at frequencies up to 1.25 Hz and amplitudes down to 10 ppm from biased FTIR measurements. Amplitudes of estimated composition profiles from the UKF are closer to the true amplitudes than those from unfiltered FTIR measurements, which lag the true profile due to residence time effects.

- The UKF yields quantitative improvements in the estimated sample profile for spline profiles of varying average amplitudes and fluctuation duration. On average, the UKF yields a 32% improvement in estimated inlet composition over unfiltered FTIR measurements across all spline profiles and flow rates tested. More accurate estimations are obtained for profiles with fluctuations of greater duration and magnitude, due to residence time and measurement noise effects, respectively.

- Measurement and estimated inlet composition improvements of 10% and 8% are achieved on average for the spline profiles, respectively, when increasing flow rate from 12 to 25 slpm. An overwhelming majority of the emissions measurement literature reports flow rates near 10 slpm. The results from this study indicate that for future emissions measurements, sample flow rate should be maximized while still maintaining appropriate pressures within the FTIR gas cell and avoiding turbulence effects.

- The relationship between an IR spectrum calculated from an interferogram from a transient measurement and the true composition profile during a measurement is exceedingly complicated. Many simplifying assumptions are invoked in the current measurement model for

tractability. Further rigor is required to achieve a robust relationship between gas cell composition and FTIR measurements that is applicable to a wider range of species and transients.

Appendix

FTIR Measurement Model Derivation

Commercial FTIRs use the Beer–Lambert law/calibration to deduce chemical composition of a sample from its spectral absorbance of IR radiation. However, the relationship between spectral absorbances/intensities calculated from a Fourier transform and chemical composition for a sample with evolving composition, and therefore transient absorbance, is complicated. The calculated spectral intensity from such a measurement is a convoluted function of the profile of intensity relative to optical path difference of the split beams within the Michelson interferometer. Therefore, transient effects must be considered in the FTIR measurement model to deduce the correct composition of an evolving sample. A measurement model is derived for a uniformly broadened spectral line with an intensity that changes linearly with respect to optical path difference. Illustrated in Figure 12 is the intensity profile of this spectrum. The remainder of the Appendix is dedicated to the derivation and discussion of the measurement model.

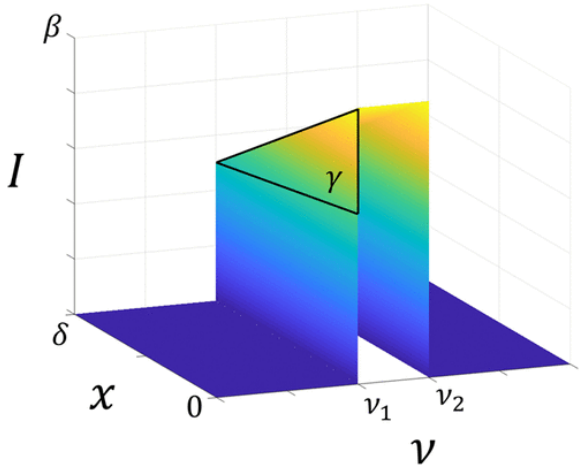

Figure 12. A uniformly broadened spectral line with linearly diminishing amplitude with respect to optical path difference.

Intensity (I) of the broadened spectral line of the line takes on a value of β at the centerburst location. It evolves with a slope of γ with respect to optical path difference (x), whose maximum value (δ). Since only the region containing the broadened spectral line is of interest, intensities outside this region are assigned a value of zero to simplify analysis. It is well known that the Fourier transform of the product of two functions is the convolution of the Fourier transform of each function. Therefore, the effect of linear evolution on the calculated spectral intensity manifests itself as a convolution of the Fourier transform of the linear profile with a unit, uniform spectrum, as shown in eq 4. By neglecting phase errors within the interferogram, which are usually corrected for in commercial FTIRs,[34] the Fourier transform becomes equivalent to the cosine transform.

$$\hat{I}(\nu) = 2\int_0^{\infty} (\beta + \gamma x)\cos(2\pi\nu x)\,dx * \frac{1}{2}\left[\prod\nolimits_{\nu_1,\nu_2}(\nu) + \prod\nolimits_{-\nu_2,-\nu_1}(\nu)\right]$$

(4)

Π is the square function, which has a value of 1 when the wavenumber (ν) is between the two subscripted values and is zero otherwise.

FTIRs can only scan to a finite optical path difference. Therefore, the upper limit of the integral in eq 4 is δ for a truncated interferogram. Furthermore, commercial FTIRs multiply the interferogram by an apodization function to mitigate spectral artifacts that emerge due to truncation. The triangular apodization function is employed for this analysis due to its abundance in the literature and similarity to more complicated functions that are used in commercial FTIRs, such as the Norton-Beer functions. The calculated spectrum from an FTIR interferogram generated by the broadened line in Figure 12 is given in eq 5.

$$\begin{aligned}\hat{I}(\nu) &= 2\int_{\delta}^{0} (\beta + \gamma x)\left(1 - \frac{x}{\delta}\right)\cos(2\pi\nu x)\,dx * \frac{1}{2}\left[\prod\nolimits_{\nu_1,\nu_2}(\nu) + \prod\nolimits_{-\nu_2,-\nu_1}(\nu)\right] \\ &= 2\left[\frac{(\beta + \gamma\delta) - (\beta + \gamma\delta)\cos(2\pi\nu\delta)}{4\delta\pi^2\nu^2} + \frac{\gamma\sin(2\pi\nu\delta)}{4\delta\pi^3\nu^3}\right] \\ &* \frac{1}{2}\left[\prod\nolimits_{\nu_1,\nu_2}(\nu) + \prod\nolimits_{-\nu_2,-\nu_1}(\nu)\right]\end{aligned}$$

(5)

The latter square function $\prod_{-\nu_2,-\nu_1}(\nu)$ turns out to contribute minimally to the estimated spectral intensity in the wavenumber range at which typical FTIR measurements are performed (700 $cm^{-1}$to 4000 cm^{-1}). Neglecting this term yields the final equation for estimated spectral intensity, where *Si* represents the sine integral.

$$\begin{aligned}\hat{I}(\nu) = \frac{\beta}{2\pi}&\left[Si\big(2\pi\delta(\nu - \nu_1)\big) - Si\big(2\pi\delta(\nu - \nu_2)\big)\right] \\ &+ \frac{\beta}{4\pi^2\delta}\left[\frac{\cos\big(2\pi\delta(\nu - \nu_1)\big)}{\nu - \nu_1} - \frac{\cos\big(2\pi\delta(\nu - \nu_2)\big)}{\nu - \nu_2}\right] \\ &+ \frac{\gamma\delta - \beta}{4\pi^2\delta}\left[\frac{1}{\nu - \nu_1} - \frac{1}{\nu - \nu_2}\right] \\ &+ \frac{\gamma}{8\pi^3\delta}\left[\frac{\sin\big(2\pi\delta(\nu - \nu_2)\big)}{(\nu - \nu_2)^2} - \frac{\sin\big(2\pi\delta(\nu - \nu_1)\big)}{(\nu - \nu_1)^2}\right]\end{aligned}$$

(6)

While complicated, this equation offers some interesting insight into the effects of Fourier transforming a transient signal. For example, as both maximum optical path difference and line width increase, the

first term becomes dominant, and the calculated spectral energy becomes more heavily weighted by the intensity at the centerburst (β), explaining the biased measurements displayed in Figure 3.

To develop a measurement model for estimating the true gas cell composition from FTIR output, values for maximum optical path difference and line width must be known/assumed. Maximum optical path difference for the MKS-2030 HS FTIR is 2 cm. The appropriate choice for line width is more ambiguous. Collision (or Lorentz) broadening is the dominant contributor to the spectral line shape of infrared absorbing gases at atmospheric temperatures and pressures.[38] Line width is typically quantified using the full width at half height of (FWHH) of the Lorentzian absorbance region of a spectrum. FWHH varies according to absorbing gas, spectral region, and mixture constituents, but typical values lie between 0.04 and 0.1 cm^{-1}.[39] However, absorption lines are often in close proximity on a spectrum, creating wide overlapping regions.[40] For example, the entire spectrum of propylene between 2900 to 3100 cm^{-1} is within an absorbed region for a wide range of temperatures and pressures.[40] A spectral line width of 1 cm^{-1} is used for this analysis. Although somewhat arbitrary, this value greatly simplifies eq 5 and provides a compromise between gases with wide overlapping regions vs. gases with thinly broadened absorption lines that rarely overlap. Invoking the above assumptions, the estimated intensity at the absorption line ($\bar{\nu}$) becomes eq 7.

$$\hat{I}(\bar{\nu}) = \frac{\beta}{\pi} Si(2\pi) + \frac{\gamma\delta}{2\pi^2} \quad (7)$$

Equation 7 is a function of β, as well as the product of γ and δ, which is the total change in intensity throughout a scan. From here, some simple scaling arguments can be applied to yield a relationship between true composition and that calculated from a steady-state calibration. First, β is assumed be linearly proportional to the composition at the centerburst location, which will be denoted as $\mathbf{Z}_{\mathrm{cell},0}$. This assumption is reasonable, since the relationship between absorbance and composition is usually linear, and the relationship between intensity and absorbance is approximately linear for low compositions. Similarly, the total change in intensity ($\gamma\delta$) during a scan should be proportional to the change in composition ($\Delta \mathrm{Z}_{\mathrm{cell}}$). Lastly, the molar composition from a steady-state calibration ($\hat{X}$) is proportional to the calculated intensity of the line. These scaling arguments lead to the following relationship between measured molar composition and the mass composition profile during a scan.

$$\hat{X} \propto \frac{\mathrm{Z}_{\mathrm{cell},0}}{\pi} Si(2\pi) + \frac{\Delta \mathrm{Z}_{\mathrm{cell}}}{2\pi^2} \quad (8)$$

Knowing that the molar composition obtained from the steady-state calibration is correct for a steady measurement, the final equation for measured molar composition during a transient can be deduced.

$$\hat{X} = \left[\mathrm{Z}_{\mathrm{cell},0} + \frac{\Delta \mathrm{Z}_{\mathrm{cell}}}{2\pi Si(2\pi)}\right] \frac{\mathrm{MW}_{\mathrm{mix}}}{\mathbf{MW}} \quad (9)$$

Equation 9 is utilized in this work to approximate gas cell composition using biased composition values formulated from FTIR measurements and steady-state calibrations. Despite its favorable performance, many simplifying assumptions are invoked in the construction of the model which may limit its

applicability to all species, transient profiles, and FTIR spectrometers. These limitations are worth discussing to guide future improvements of the model. First, this analysis assumes a uniformly broadened spectral line. True broadened absorption lines of infrared active gases, including acetylene, are of a Lorentzian shape at typical measurement conditions.[34] A uniformly broadened spectral line is utilized because it simplifies the convolution in eq 5 and leads to a tractable equation for estimated spectral intensity. Further analysis is required to determine if considering a Lorentzian lineshape improves the fidelity of the model. Secondly, this model assumes a linear intensity profile with respect to optical path difference, while the true profile during a transient is likely more complex and time-varying. Furthermore, the measurement model implicitly assumes that time and optical path difference are linearly related, or that scan speed is constant. Moving mirrors have periods of acceleration and deceleration at the beginning and end of a scan, respectively. However, inference of the current composition from FTIR measurements of transient requires an assumed transient profile, the simplest of which is a linear one. Also, the widths of broadened absorption lines vary according to species and composition. A general line width of 1 cm^{-1} is used for this analysis, while a more rigorous approach would consider the specific spectrum of each individual species. However, the choice of 1 cm^{-1} provides a first approximation that significantly reduces the complexity of the measurement model. Lastly, the measurement model neglects the effects of interference from other species, which may differ during transients compared to steady measurements. Nevertheless, the derived measurement model provides higher quality estimates of gas cell composition than the traditional method of using steady-state calibrations, despite its simplifying assumptions.

The authors declare no competing financial interest.

Acknowledgments

The authors gratefully acknowledge the helpful input and support received from Steve Wright and Sylvie Bosch-Charpenay of MKS Instruments. The authors additionally thank Dr. Matti Maricq of Ford Motor Company for sharing his FTIR applications knowledge. Financial support from Marquette University OPUS College of Engineering is also gratefully acknowledged.

Nomenclature	
BEM	Bayesian estimation model
FTIR	Fourier transform infrared spectroscopy
MFC	mass flow controller
MFM	mass flow meter
ms	millisecond
ppm	parts per million
s	seconds
sccm	standard cubic centimeters per minute
slpm	standard liters per minute
UKF	unscented Kalman filter
VOC	volatile organic compounds
I	intensity
m	mass within gas cell
$\dot{m}$	mass flow rate
$\mathbf{MW}$	molecular weights of species of interest

M_{Wmix}	molecular weight of total gas cell sample
t	time
Si	sine integral
$\dot{V}$	volume flow rate
x	optical path difference
$\boldsymbol{x}$	system state
$\boldsymbol{y}$	measurement
$\mathbf{Z}_{\mathrm{cell}}$	mass composition within FTIR gas cell
$\mathbf{Z}_{\mathrm{cell,0}}$	mass composition within FTIR gas cell at centerburst location
$\mathbf{Z}_{\mathrm{cell,t-1}}$	mass composition within FTIR gas cell at previous time
$\mathbf{Z}_{\mathrm{in}}$	mass composition entering FTIR gas cell
β	line intensity at centerburst location
γ	slope of intensity change with respect to optical path difference
δ	maximum optical path difference
Π	square function
τ	effective FTIR gas cell time constant
ν	wavenumber
$\wedge$	calculation/estimation
$<>$	expected value

References

1. Atkinson, R. Atmospheric chemistry of VOCs and NO(x). *Atmos. Environ.* **2000**, *34* (12–14), 2063– 2101,DOI: 10.1016/S1352-2310(99)00460-4
2. Chiemchaisri, W.; Visvanathan, C.; Jy, S. W. Effects of trace volatile organic compounds on methane oxidation. *Braz. Arch. Biol. Technol.* **2001**, *44* (2), 135– 140, DOI: 10.1590/S1516-89132001000200005
3. Carslaw, K. S.; Boucher, O.; Spracklen, D. V.; Mann, G. W.; Rae, J. G. L.; Woodward, S.; Kulmala, M.Atmospheric aerosols in the earth system: a review of interactions and feedbacks. *Atmos. Chem. Phys. Discuss.* **2009**, *9* (3), 11087– 11183, DOI: 10.5194/acpd-9-11087-2009
4. Jimenez, J. L.; Canagaratna, M. R.; Donahue, N. M.; Pŕev̂ot, A. S. H.; Zhang, Q.; Kroll, J. H.; DeCarlo, P. F.;Allan, J. D.; Coe, H.; Ng, N. L.; Aiken, A. C.; Docherty, K. D.; Ulbrich, I. M.; Grieshop, A. P.; Robinson, A. L.;Duplissy, J.; Smith, J. D.; Wilson, K. R.; Lanz, V. A.; Hueglin, C.; Sun, Y. L.; Laaksonen, A.; Raatikainen, T.;Rautiainen, J.; Vaattovaara, P.; Ehn, M.; Kulmala, M.; Tomlinson, J. M.; Collins, D. R.; Cubison, M. J.;Dunlea, E. J.; Huffman, J. A.; Onasch, T. B.; Alfarra, M. R.; Williams, P. I.; Bower, K.; Kondo, Y.;Schneider, J.; Drewnick, F.; Borrmann, S.; Weimer, S.; Demerjian, K.; Salcedo, D.; Cottrell, L.; Griffin, R.;Takami, A.; Miyoshi, T.; Hatakeyama, S.; Shimono, A.; Sun, J. Y.; Zhang, Y. M.; Dzepina, K.; Kimmel, J. R.;Sueper, D.; Jayne, J. T.; Herndon, S. C.; Trimborn, A. M.; Williams, L. R.; Wood, E. C.; Kolb, C. E.;Baltensperger, U.; Worsnop, D. R.; Middlebrook, A. M.; Tian, J. Evolution of Organic Aerosols in the Atmosphere: A New Framework Connecting Measurements to Models. *Science (Washington, DC, U. S.)***2009**, *326* (5959), 1525– 1529, DOI: 10.1126/science.1180353
5. Olumayede, E. G. Atmospheric Volatile Organic Compounds and Ozone Creation Potential in an Urban Center of Southern Nigeria. *Int. J. Atmos. Sci.* **2014**, *2014*, 1– 7, DOI: 10.1155/2014/764948
6. Atkinson, R. *Kinetics and Mechanisms of the Gasphase Reactions of the Hydroxyl Radical with Organic Compounds*; American Chemical Society, **1989**.

7. Kampa, M.; Castanas, E. Human health effects of air pollution. *Environ. Pollut.* **2008**, *151*, 362– 367, DOI: 10.1016/j.envpol.2007.06.012
8. Bahadar, H.; Mostafalou, S.; Abdollahi, M. Current understandings and perspectives on non-cancer health effects of benzene: A global concern. *Toxicol. Appl. Pharmacol.* **2014**, *276*, 83– 94, DOI: 10.1016/j.taap.2014.02.012
9. U.S. Environmental Protection Agency, "Profile of version 1 of the 2014 National Emissions Inventory," **2017**. [Online]. Available: https://www.epa.gov/sites/production/files/2017-04/documents/2014neiv1_profile_final_april182017.pdf. [Accessed: 01-Jun-2017].
10. von Schneidemesser, E.; Monks, P. S.; Plass-Duelmer, C. Global comparison of VOC and CO observations in urban areas. *Atmos. Environ.* **2010**, *44*, 5053– 5064, DOI: 10.1016/j.atmosenv.2010.09.010
11. Rakopoulos, C. D.; Dimaratos, A. M.; Giakoumis, E. G.; Rakopoulos, D. C. Evaluation of the effect of engine, load and turbocharger parameters on transient emissions of diesel engine. *Energy Convers. Manage.* **2009**, *50*, 2381– 2393, DOI: 10.1016/j.enconman.2009.05.022
12. Hagena, J. R.; Filipi, Z. S.; Assanis, D. N. Transient Diesel Emissions: Analysis of Engine Operation During a Tip-In. *SAE Technol. Pap.* **2006**
13. Ericsson, E. Variability in urban driving patterns. *Transp. Res. Part D Transp. Environ.* **2000**, *5*, 337– 354,DOI: 10.1016/S1361-9209(00)00003-1
14. Poulopoulos, S. G.; Samaras, D. P.; Philippopoulos, C. J. Regulated and unregulated emissions from an internal combustion engine operating on ethanol-containing fuels. *Atmos. Environ.* **2001**, *35*, 4399– 4406,DOI: 10.1016/S1352-2310(01)00248-5
15. Corrêa, S. M.; Arbilla, G. Aromatic hydrocarbons emissions in diesel and biodiesel exhaust. *Atmos. Environ.***2006**, *40*, 6821– 6826, DOI: 10.1016/j.atmosenv.2006.05.068
16. Tsai, J. H.; Chiang, H. L.; Hsu, Y. C.; Weng, H. C.; Yang, C. Y. The speciation of volatile organic compounds (VOCs) from motorcycle engine exhaust at different driving modes. *Atmos. Environ.* **2003**, *37*, 2485– 2496,DOI: 10.1016/S1352-2310(03)00177-8
17. Machado Corrêa, S.; Arbilla, G. Carbonyl emissions in diesel and biodiesel exhaust. *Atmos. Environ.* **2008**,*42*, 769– 775, DOI: 10.1016/j.atmosenv.2007.09.073
18. Manning, C. J.; Griffiths, P. R. Noise Sources in Step-Scan FT-IR Spectrometry. *Appl. Spectrosc.* **1997**, *51*,1092– 1101, DOI: 10.1366/0003702971941755
19. Gierczak, C. A.; Kralik, L. L.; Mauti, A.; Harwell, A. L.; Maricq, M. M. Measuring NMHC and NMOG emissions from motor vehicles via FTIR spectroscopy. *Atmos. Environ.* **2017**, *150*, 425– 433, DOI: 10.1016/j.atmosenv.2016.11.038
20. Li, H.; Andrews, G. E.; Savvidis, D.; Daham, B.; Ropkins, K.; Bell, M.; Tate, J. Comparisons of the Exhaust Emissions for Different Generations of SI Cars under Real World Urban Driving Conditions. *SAE Tech. Pap. Ser.* **2008**, DOI: 10.4271/2008-01-0754
21. Daham, B.; Andrews, G.; Li, H.; Ballesteros, R.; Bell, M.; Tate, J.; Ropkins, K. Application of a portable FTIR for measuring on-road emissions. *SAE Tech. Pap. Ser.* **2005**, DOI: 10.4271/2005-01-0676
22. Szybist, J. P.; Boehman, A. L.; Haworth, D. C.; Koga, H. Premixed ignition behavior of alternative diesel fuel-relevant compounds in a motored engine experiment. *Combust. Flame* **2007**, *149*, 112– 128, DOI: 10.1016/j.combustflame.2006.12.011
23. Truex, T. J.; Collins, J. F.; Jetter, J. J.; Knight, B.Measurement of Ambient Roadway and Vehicle Exhaust Emissions – An Assessment of Instrument Capability and Initial On-Road Test Results with an Advanced Low Emission Vehicle. *SAE Tech. Pap. Ser.* **2000**, DOI: 10.4271/2000-01-1142

24. Wallner, T.; Frazee, R. Study of regulated and non-regulated emissions from combustion of gasoline, alcohol fuels and their blends in a DI-SI engine. *SAE Technol. Pap.* **2010**
25. Bielaczyc, P.; Woodburn, J.; Klimkiewicz, D.; Pajdowski, P.; Szczotka, A. An examination of the effect of ethanol-gasoline blends' physicochemical properties on emissions from a light-duty spark ignition engine.*Fuel Process. Technol.* **2013**, *107*, 50– 63, DOI: 10.1016/j.fuproc.2012.07.030
26. Suarez-Bertoa, R.; Zardini, A. A.; Astorga, C. Ammonia exhaust emissions from spark ignition vehicles over the New European Driving Cycle. *Atmos. Environ.* **2014**, *97*, 43– 53, DOI: 10.1016/j.atmosenv.2014.07.050
27. Suarez-Bertoa, R.; Zardini, A. A.; Lilova, V.; Meyer, D.; Nakatani, S.; Hibel, F.; Ewers, J.; Clairotte, M.;Hill, L.; Astorga, C. Intercomparison of real-time tailpipe ammonia measurements from vehicles tested over the new world-harmonized light-duty vehicle test cycle (WLTC). *Environ. Sci. Pollut. Res.* **2015**, *22*, 7450–7460, DOI: 10.1007/s11356-015-4267-3
28. Huang, N.; Shen, Z.; Long, S.; Wu, M.; Shih, H.; Zheng, Q.; Yen, N.; Tung, C.; Liu, H. The empirical mode decomposition and the Hilbert spectrum for nonlinear and non-stationary time series analysis. *Proc. R. Soc. London, Ser. A* **1998**, *454*, 903, DOI: 10.1098/rspa.1998.0193
29. Huai, T.; Durbin, T. D.; Wayne Miller, J.; Norbeck, J. M. Estimates of the emission rates of nitrous oxide from light-duty vehicles using different chassis dynamometer test cycles. *Atmos. Environ.* **2004**, *38*, 6621– 6629,DOI: 10.1016/j.atmosenv.2004.07.007
30. Wilson, D.; Allen, C. A Bayesian Estimation Model for Transient Engine Exhaust Characterization Using Fourier Transform Infrared Spectroscopy. *Energy Fuels* **2017**, *31*, 11156, DOI: 10.1021/acs.energyfuels.7b02224
31. Candy, J. V. *Bayesian Signal Processing: Classical, Modern, and Particle Filtering Methods*; John Wiley and Sons: Hoboken, NJ, **2016**.
32. Wan, E. A.; van der Merwe, R. The unscented Kalman filter for nonlinear estimation. In *Proceedings of the IEEE 2000 Adaptive Systems for Signal Processing, Communications, and Control Symposium*, **2000**.
33. Julier, S. J.; Uhlmann, J. K. A New Extension of the Kalman Filter to Nonlinear Systems. In *Proceedings of AeroSense: The 11th International Symposium on Aerospace/Defence Sensing, Simulation and Controls*,**1997**.
34. Griffiths, P. R.; De Haseth, J. A. *Fourier Transform Infrared Spectrometry*; John Wiley & Sons Inc.: New York, **1986**.
35. Zhang, F.; Wang, J.; Tian, D.; Wang, J.-X.; Shuai, S.-J. Research on Unregulated Emissions from an Alcohols-Gasoline Blend Vehicle Using FTIR, HPLC and GC-MS Measuring Methods. *SAE Int. J. Engines,* **2013**, *6* (no. 2), 2013– 01–1345
36. Penteado, R.; Daemme, L.; Melo, T. An Experimental Investigation on Regulated and Unregulated Emissions from Four 4-Stroke Gasoline-Powered Motorcycle, **2012**.
37. Peckham, M. S.; Finch, A.; Campbell, B. Analysis of Transient HC, CO, NOx and CO_2 Emissions from a GDI Engine using Fast Response Gas Analyzers. *SAE Int. J. Engines* **2011**, *4* (no. 1), 2011-01-1227
38. Modest, M. F. *Radiative Heat Transfer*, 3rd ed.; Academic Press: Oxford, **2013**.
39. Ludwig, C. B.; Malkmus, W.; Reardon, J. E.; Thomson, J. A. L. *Handbook of Infrared Radiation from Combustion Gases*; Washington, D.C., **1973**.
40. Buzan, E. M.; Hargreaves, R. J.; Bernath, P. F. High resolution absorption cross sections for propylene in the 3 μm region at high temperatures. *Mol. Astrophys.* **2016**, *3–4*, 16– 20, DOI: 10.1016/j.molap.2016.06.001